ECCOMAS Congress 2016
VII European Congress on Computational Methods in Applied Sciences and Engineering
M. Papadrakakis, V. Papadopoulos, G. Stefanou, V. Plevris (eds.)
Crete Island, Greece, 5–10 June 2016

A METHOD OF CHAINED ANALYTICAL WAVE STRUCTURES FOR LARGE-SCALE STRATIFIED TWO-PHASE PIPE FLOWS (ECCOMAS CONGRESS 2016)

A.H. Akselsen[1]

[1]Department of Energy and Process Engineering, Norwegian University of Science and Technology
Kolbjørn Hejes v. 1B, 7491 Trondheim, Norway
e-mail: andreas.h.akselsen@ntnu.no

Keywords: Chained Analytical Waves; Roll-Waves; Two-Phase Flow; Pipe Flow; Two-Fluid Model

Abstract. *Pipeline transport systems can span vast distances, making finely resolved simulation techniques computationally unaffordable. This article examines the use of analytical steady wave solutions in a dynamic simulation framework as a technique for obtaining physical wave dynamics in a flow regime simulator without discretising individual wave structures. A scheme based on this principle is presented wherein a family of steady roll-waves profile solutions is generalised to allow for a dynamic profile evolution. These solutions are then implemented into a finite volume scheme where a wave solution constitutes a single dynamic grid cell. Waves interact dynamically to construct a wave regime evolving in time. Predictions on flow development are compared with finely resolved direct numerical simulations on fixed grids. Steady wave solutions, once subjected to coordinate stretching, behaves appropriately in the dynamic frame, predicting the regime development in time, the wave coalescences and the final steady state or slug transition.*

1 INTRODUCTION

1.1 Review

Roll-wave trains are periodic occurrences of moving hydraulic jumps and constitutes a shallow-water flow regime in both channels and pipes. The wave dynamic of this flow regime is important in two-phase pipe flows as it affect the momentum exchange between phases, and because it may initiate the transition to a slugging flow.

Profile solutions of steady-state hydraulic jumps in open channels was published by Brass already in 1868.

Thomas [17] presented, in 1937 and 1939, a family of explicit, mechanistic, free surface roll-wave solutions using a reference system relative to the waves through a moving belt analogy.

Dressler [7] later formalised these profile solutions into a closed form composed of trains of piecewise monotonic solutions connected by shocks. He formulated conservation conditions for these shocks. Dressler also went on to prove the uniqueness of these solutions through entropy considerations, and to also construct viscous, continuous profile solutions. Thomas and Dressler both showed, by different means, that some amount of friction was a necessary requirement for the formation of roll-waves.

Miya et. al. [14] went on to derive similar profile solutions for gas-liquid channel flows, also including shape factors for the velocity profiles. They further investigated the pressure distribution and compared the profile solutions to experimental data.

Watson [18] reformulated the gas-liquid solution for flow in pipes. This model had a form similar to that for channel flow, but with a geometrical complexity making it unsuited for analytical integration. Algebraically explicit profile solutions are therefore unavailable for pipe flow. The increased complexity of these equations also makes solution uniqueness difficult to prove; this was instead assumed.

Johnson et. al. [11, 10] continued the work on discontinuous and viscous continuous roll-wave models for stratified pipe flow. They constructed a database system for retrieving profile solutions at given flow conditions. In [12], Johnson et. al. compare high-pressure, upward inclined pipe flow experiments to the continuous roll-wave model to find good agreement.

Comparisons between roll-wave experiments and predictions from finely resolved numerical representations have been made by multiple authors. For instance, Holmås [9] compared a pseudospectral representation (using fast Fourier transformation) of the incompressible two-fluid pipe flow model with the above cited experiments of Johnson. The Biberg model [2] for pre-integrated turbulent shear and velocity profiles was here incorporated.

Similar comparisons were made by Cao et. al. [5], including $k-\varepsilon$ turbulent closures to their Riemann solver + MUSCL method. They report good agreement with the experimental data of Brock's [3] after the $k-\varepsilon$ extension.

Richard and Gavrilyuk [15] extended Dressler's roll-wave solutions to account for turbulent shear and dissipation. Reynolds' stresses are here related to enstrophy in the wave, providing wave-breaking as a model extension. Very good agreement with Brock's experimental data was found [3], appropriately breaking off the sharp wave tip of the Dressler solutions.

In the work of Brook et. al. [4], the solutions of Dressler were compared to roll-wave simulation results of the shallow water equations using a second order Godunov method.

A final work worth mentioning in relation to these steady wave solutions is Lahey's piece on dispersed bubbly pipe flow [13]. Here, void waves were analysed using non-linear theory, finding similar sets of structures and profile solutions.

In regard to the method principle, some ideas have been drawn from the work of De Leebeeck

and Nydal [6]. They presented a phenomenological model treating large waves as a fixed-length choke object and used object oriented programming to simulate intermittent occurrences of such wave representations.

1.2 Aim

The aim in this work is to whether solutions for steady wave trains can be used in modelling dynamically evolving wavy flows. Will a set of spurious analytical waves merge and adjust to a 'fully developed' flow pattern? Does the method have potential for use in engineering simulator tools?

The concept is tested through a method based on the principle of singleton wave solutions in the frame of a finite volume method. Predicting the development of a *flow regime* in long pipeline simulations is usually more important than predicting individual waves. We need therefore not demand exact conformity with the base model, but that the appropriate statistical development is ensured and that predictions on regime transition are reliable. Similar methods can be devised for any type of regime flow where reasonably steady intermittent structures appear.

1.3 Introduction to a method of dynamically chained analytical wave structures

In this article, the steady state solutions presented by the aforementioned authors will be generalised and introduced into a dynamic, computational framework for simulating transient wave development. (The term 'steady state' will here refere to solutions which are steady in a reference system moving with constant translation velocity.) For ease of reference, the resulting method will be dubbed *the method of chained analytical waves,* CAW for short.

The concept of the CAW method is presented in Figure 1.1 with explanations in the caption. It consists of four basic steps:

i) A profile and shock celerity reconstruction from the average state properties in a relative reference system.

ii) Integrating the average wave properties in time using fluxes and sources obtained from the chained profiles.

iii) Letting the wave objects move according to the shock celerities.

iv) Reconstructing the profiles and shock celerities anew from the new average properties.

The two-fluid model is presented in Section 2. A conservative finite volume method for dynamic cells is then presented in Section 3.1, with the average volume equations in Section 3.1.1 and the shock conditions in Section 3.1.2. The analytical wave model is found in Section 3.2, with the general profile equations presented in Section 3.2.2. Section 3.3 deals with selecting a wave profile from the family of profile solutions on the basis of the average properties. Putting these pieces together, Section 3.4 presents the simulation routine.

Figure 1.2 illustrates the main difference between the CAW method and conventional, fine-gridded CFD methods, namely the much greater number of grid cells required by the latter. The numerical stability of both types of solution methods will be restricted by CFL-type criteria which limit the length of the time integration step in proportion to the grid cell lengths. Consequently, the CAW method should be capable of remaining stable while using significantly longer time steps, at a time scale better suited for wave dynamics.

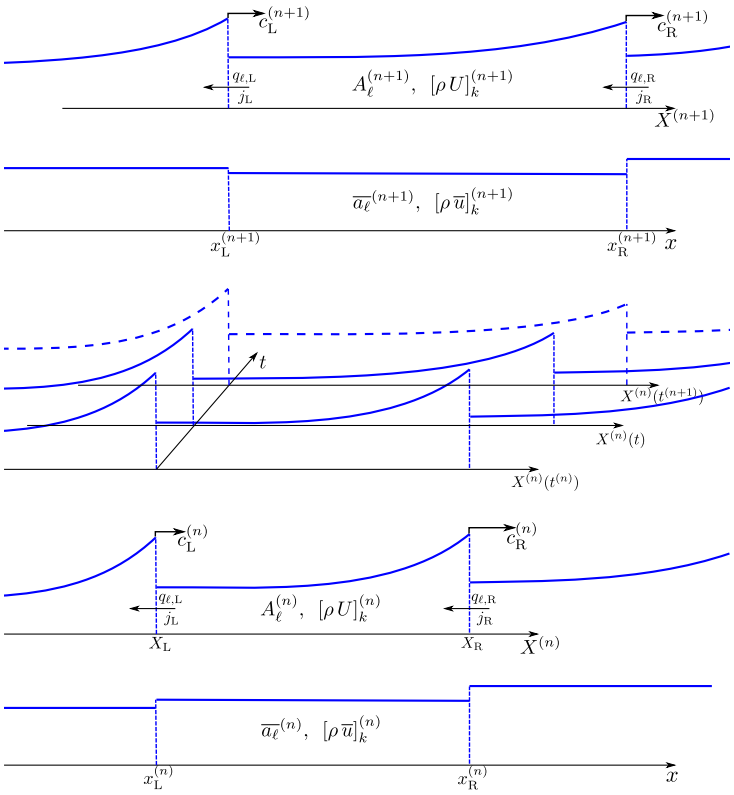

Figure 1.1: Principle illustration.
• Bottom: Available average state $\overline{\boldsymbol{\psi}}$
• 2nd from bottom: Adopt a reference system relative to the wave. Reconstruct the waves with the analytical wave model and determine the shock celerities and the flux exchanges between waves (Section 3.2-3.3.)
• Middle: Integrate in time using the fluxes and shock speeds obtained at $t^{(n)}$ from the analytical wave regime. Allow the wave to stretch and contract in the strip $t \in \left[t^{(n)}, t^{(n+1)}\right\rangle$, (Section 3.1.)
• 2nd from top and top: The time integration provides the average state $\overline{\boldsymbol{\psi}}^{(n+1)}$ at time $t^{(n+1)}$, and the cycle repeats for the new time step.

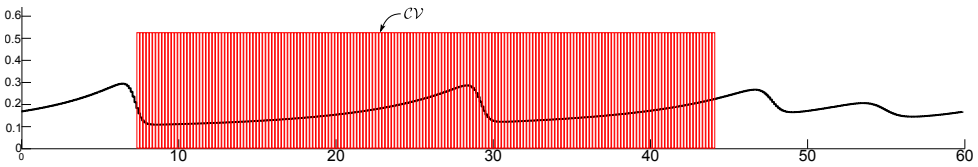

(a) Conventional capturing simulation with a fine, stationary grid – 500 grid cells.

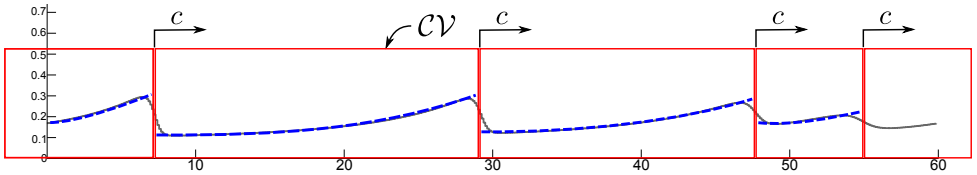

(b) Chained analytical wave simulation – 4 grid cells.

Figure 1.2: Control volumes

2 THE TWO-FLUID MODEL

In addition to the presence of a gas, the complication of a pipe geometry is a key difference between the explicit shallow water roll-wave solutions of Dressler and the numerically computed pipe flow solutions of Watson – Figure 2.1 shows a schematic. The pipe introduces new

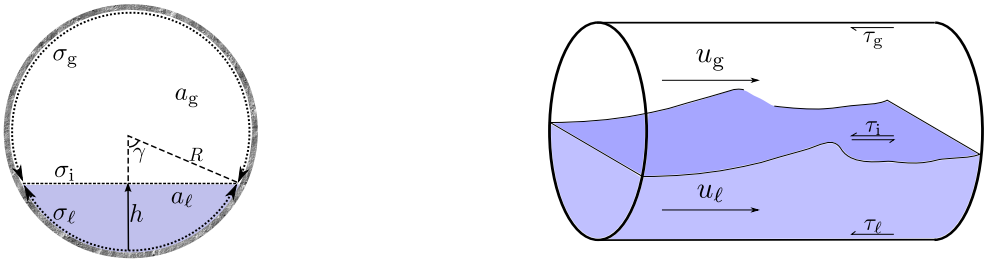

Figure 2.1: Pipe cross-section

geometric variables such as the level height h, partial cross-section areas a_k and perimeter length σ_k for the gas ($k = \mathrm{g}$) and liquid ($k = \ell$) phases. These are all algebraically interchangeable through a geometric function $a_\ell = \mathcal{A}_\ell(h)$:

$$\mathcal{A}_\ell(h) = R^2\left(\gamma - {}^1\!/_2 \sin 2\gamma\right), \qquad \sigma_\ell = 2R\gamma,$$
$$\mathcal{A}'_\ell = \frac{\mathrm{d}\mathcal{A}_\ell}{\mathrm{d}h} = \sigma_\mathrm{i}, \qquad \sigma_\mathrm{g} = 2R\left(\pi - \gamma\right),$$
$$\gamma = \arccos\left(1 - h/R\right), \qquad \sigma_\mathrm{i} = 2R\sin\gamma.$$

Though expressions of the same property, the level height h is beat suited as an independent modelling variable as a_k and σ_k are explicit functions in h, whereas the inverse is not true. R is here the pipe inner radius and γ the interface half-angle. Subscript 'i' indicates the gas-liquid interface.

The compressible, isothermal, four-equation two-fluid model for stratified pipe flow results from an averaging of the conservation equations across the cross-sectional area and is commonly written

$$\partial_t\left(a\rho\right)_k + \partial_x\left(a\rho u\right)_k = 0, \tag{2.1a}$$
$$\partial_t\left(a\rho u\right)_k + \partial_x\left(a\rho u^2\right)_k + a_k\partial_x p_\mathrm{i} + a_k\rho_k g\cos\theta\,\partial_x h = s_k, \tag{2.1b}$$

where phase subscript $k \in \{\mathrm{g}, \ell\}$. p_i is the interface pressure, coupled to the fluid densities ρ_k by some equation of state.

The phase properties represent cross-sectional averages in each field, and, together, the two last left-hand terms in the momentum equation represents a hydrostatic approximation to the average pressures over the cross-section. A flat, fully turbulent velocity profile is here assumed.

The numerical treatment of the pressure term is a key issue in simulating the two-fluid model. It introduces sonic characteristics and stability restrictions. In this work, as well as in most of those hereto cited, pressure issues are numerically sidestepped by assuming both phases to be incompressible. This eliminates the sonic characteristics while the system still retains its conditionally hyperbolic nature. It also allows for a conservative, two-equation system formulation. The interfacial pressure, essentially linking the momentum equations of each phase, is eliminated by first reducing each momentum equation by their respective mass equations, and then

divided each by their respective specific areas a_k. Subtracting one from the other, the pressure term is eliminated. The resulting conservation equations reads

$$\partial_t \boldsymbol{\psi} + \partial_x \boldsymbol{f} = \boldsymbol{s} \tag{2.2a}$$

with

$$\boldsymbol{\psi} = \begin{pmatrix} a_\ell \\ [\rho u]^\ell_{\mathrm{g}} \end{pmatrix}, \qquad \boldsymbol{f} = \begin{pmatrix} q_\ell \\ j \end{pmatrix}, \qquad \boldsymbol{s} = \begin{pmatrix} 0 \\ s \end{pmatrix}. \tag{2.2b}$$

Flux and source component symbols have here been introduced and are

$$q_k = a_k u_k, \qquad j = \left[\rho \frac{u^2}{2}\right]^\ell_{\mathrm{g}} + w_y\, h, \tag{2.2c}$$

$$s = -w_x - \left[\frac{\tau\sigma}{a}\right]^\ell_{\mathrm{g}} + \tau_{\mathrm{i}}\sigma_{\mathrm{i}}\left(\frac{1}{a_\ell} + \frac{1}{a_{\mathrm{g}}}\right), \tag{2.2d}$$

and phase differencing operation $[\cdot]^\ell_{\mathrm{g}} = (\cdot)_\ell - (\cdot)_{\mathrm{g}}$ which will be used throughout. The algebraic relations

$$a_\ell + a_{\mathrm{g}} = \mathcal{A}, \qquad q_\ell + q_{\mathrm{g}} = \mathcal{Q}, \tag{2.2e}$$

close the model. This is essentially the same formulation as used by Holmås in [9]. $\mathcal{A}$ may in general be a parametric function of x and $\mathcal{Q}$ of t, though they are here treated as constants. The second relation in (2.2e) is obtained from adding together the two mass equations (2.1a) and applying the first relation. Specific weight terms, also parametric, are

$$w_x = [\rho]^\ell_{\mathrm{g}}\, g \sin\theta, \qquad w_y = [\rho]^\ell_{\mathrm{g}}\, g \cos\theta,$$

with g being the gravitational acceleration and θ the pipe inclination angle, positive above datum. The friction model τ_k is based on the rather simple Taitel and Dukler model [16] for turbulent flow, quickly summarised below:

$$\begin{aligned} &\tau_k = {}^1\!/_2\, C_{\mathrm{f},k}\, \rho_k u_k |u_k|, && \tau_{\mathrm{i}} = {}^1\!/_2\, C_{\mathrm{f,i}}\, \rho_{\mathrm{g}} (u_{\mathrm{g}} - u_\ell)|u_{\mathrm{g}} - u_\ell|, \\ &C_{\mathrm{f},k} = 0.046\, Re_k^{-0.2}, && Re_k = (ud/\nu)_k, \\ &d_\ell = 4\, a_\ell/\sigma_\ell, && d_{\mathrm{g}} = 4\, a_{\mathrm{g}}/(\sigma_\ell + \sigma_{\mathrm{i}}). \end{aligned}$$

The interfacial friction factor is $C_{\mathrm{f,i}} = m_{\mathrm{x}} \max\{C_{\mathrm{f,g}}, 0.014\}$ where m_{x} is a crude model parameter employed by numerous authors in order to achieve $C_{\mathrm{f,i}} > C_{\mathrm{f,g}}$ as observed experimentally. ν is the kinematic viscosity.

A study on how m_{x} affect the wave regime was carried out in [11] and will not be repeated here. Instead, m_{x} is rather arbitrarily given the value $m_{\mathrm{x}} = 5.0$. The choice of m_{x} affects the range of flow conditions in which the stable roll-wave regime is observed.

3 A METHOD OF CHAINED ANALYTICAL WAVE STRUCTURES

Details of the CAW method are described in this section. The process of averaging the base equation system (2.2) into movable, stretching and contracting control volumes is described in Subsection 3.1, while details of the wave model are described in Subsection 3.2. Finally, a routine description is given in Subsection 3.4.

Readers who are foremost interested in the method principle (as presented in the introductory section) may skip past the method details presented here and still gather an impression from the results section that follows.

3.1 A finite volume method framework

3.1.1 Average volume equations

A control volume is placed over a wave, as illustrated in Figure 1.2b. Integration of (2.2a) is performed across the control volume, first in space from the left shock at x_{L} to the right one at x_{R}, and then in time from the present time t_n to the next time level t_{n+1}:

$$\int_{t_n}^{t_{n+1}} \int_{x_{\mathrm{L}}(t)}^{x_{\mathrm{R}}(t)} \left(\partial_t \boldsymbol{\psi} + \partial_x \boldsymbol{f} - \boldsymbol{s}\right) \mathrm{d}x \, \mathrm{d}t = 0. \tag{3.1}$$

Using Leibniz' rule, the first transient term evaluates to

$$\int_{x_{\mathrm{L}}(t)}^{x_{\mathrm{R}}(t)} \partial_t \boldsymbol{\psi} \, \mathrm{d}x = \partial_t \big(\Delta x \overline{\boldsymbol{\psi}}\big) - \left[c \, \boldsymbol{\psi}\right]_{\mathrm{L}}^{\mathrm{R}} \tag{3.2}$$

where $c = \frac{\mathrm{d}x}{\mathrm{d}t}$ is the control volume border velocity, chosen equal to the shock speed of the wave front discontinuity, such that the control volume follows the wave front. $\Delta x(t) = x_{\mathrm{R}}(t) - x_{\mathrm{L}}(t)$ is the wavelength, and the notation for evaluating the left-right difference $[\cdot]_{\mathrm{L}}^{\mathrm{R}} = (\cdot)_{\mathrm{R}} - (\cdot)_{\mathrm{L}}$ is adopted. The bar will indicate the cell average and is defined

$$\overline{\phi}(t) = \frac{1}{\Delta x(t)} \int_{x_{\mathrm{L}}(t)}^{x_{\mathrm{R}}(t)} \phi(x,t) \, \mathrm{d}x. \tag{3.3a}$$

Also introducing the temporal average $\langle \cdot \rangle^{(n)}$,

$$\big\langle \phi(x) \big\rangle^{(n)} = \frac{1}{\Delta t} \int_{t_n}^{t_{n+1}} \phi(x,t) \, \mathrm{d}t \tag{3.3b}$$

with $\Delta t = t_{n+1} - t_n$, the integral equation (3.1) is cast as

$$\big(\Delta x \overline{\boldsymbol{\psi}}\big)^{(n+1)} = \big(\Delta x \overline{\boldsymbol{\psi}}\big)^{(n)} + \Delta t \left\langle \Delta x \overline{\boldsymbol{s}} - [\boldsymbol{f}_{\mathrm{r}}]_{\mathrm{L}}^{\mathrm{R}} \right\rangle^{(n)}, \tag{3.4}$$

where the flux terms have been made relative to the shock propagation, i.e., $\boldsymbol{f}_{\mathrm{r}} = (q_{\ell,\mathrm{r}}, j_{\mathrm{r}})^T = \boldsymbol{f} - c\boldsymbol{\psi}$. Relative notation will be adopted throughout to indicate when fluxes are relative a moving frame. The mass and momentum fluxes of the relative frame are key variables and are therefore emphasised:

$$q_{\ell,\mathrm{r}} = a_\ell \left(u_\ell - c\right), \qquad\qquad j_{\mathrm{r}} = \left[\rho u \left(\frac{u}{2} - c\right)\right]_{\mathrm{g}}^{\ell} + h w_y. \tag{3.5}$$

It is important to note that Equation (3.4) is still exact.

In case of a first order time integration, $\langle \cdot \rangle^{(n)}$ simply evaluates to

$$\langle \cdot \rangle^{(n)} \xrightarrow{\text{explicit}} (\cdot)^{(n)}, \qquad\qquad \langle \cdot \rangle^{(n)} \xrightarrow{\text{implicit}} (\cdot)^{(n+1)}.$$

Explicit time integration $\langle \cdot \rangle^{(n)} \to (\cdot)^{(n)}$ is used in the CAW method. Equation (3.4) then reads

$$\begin{aligned}
\left(\Delta x \overline{a_\ell}\right)^{(n+1)} &= \left(\Delta x \overline{a_\ell}\right)^{(n)} - \Delta t \left[q_{\ell,\mathrm{r}}^{(n)}\right]_{\mathrm{L}}^{\mathrm{R}}, \\
\left(\Delta x \left[\rho \overline{u}\right]_{\mathrm{g}}^{\ell}\right)^{(n+1)} &= \left(\Delta x \left[\rho \overline{u}\right]_{\mathrm{g}}^{\ell}\right)^{(n)} + \Delta t \left(\Delta x \overline{s} - [j_{\mathrm{r}}]_{\mathrm{L}}^{\mathrm{R}}\right)^{(n)}.
\end{aligned}$$

3.1.2 Shock conditions

The coordinate translation velocity $C(H)$ may dynamically vary over a wave as it stretches or contracts, meaning that celerity c adhere to the shocks themselves rather to a wave as a whole. A shock must obey the condition that the relive fluxes $\boldsymbol{f}_{\mathrm{r}} = (q_{\ell,\mathrm{r}}, j_{\mathrm{r}})^T$ are shock invariant.[1]

Following a shock front $i + \frac{1}{2}$, the common notation for a left and right discontinuity limit is adopted, namely $\phi^- = \phi_{\mathrm{R},i}$ and $\phi^+ = \phi_{\mathrm{L},i+1}$. The conservation conditions $j_{\mathrm{r}}^- = j_{\mathrm{r}}^+$ and $q_{\ell,\mathrm{r}}^- = q_{\ell,\mathrm{r}}^+$ imply $J_{\mathrm{r}}(h^-, q_{\ell,\mathrm{r}}, c) = J_{\mathrm{r}}(h^+, q_{\ell,\mathrm{r}}, c)$. Subtracting $\frac{1}{2}\rho_k c$ on both sides illustrates that this condition corresponds to maintaining a Bernoulli invariant

$$\left[\left[\tfrac{1}{2}\rho\,(u-c)^2\right]_{\mathrm{g}}^{\ell} + w_y\, h\right]_{-}^{+} = 0, \tag{3.6}$$

where $[\cdot]_-^+ = (\cdot)^+ - (\cdot)^-$. This is the jump condition similar to that presented by Watson [18]. Solving for c yields

$$c = \frac{\left[\rho\,[u^2/2]_-^+\right]_{\mathrm{g}}^{\ell} + w_y\,[h]_-^+}{\left[\rho\,[u]_-^+\right]_{\mathrm{g}}^{\ell}}.$$

Conservation of the relative discharge $q_{\ell,\mathrm{r}}$ can be archived through the model choice of $Q_{\ell,\mathrm{r}}(H)$ – see Section 3.2.3.

Once the shock celerities and the integral values (3.4) have been computed, the control volume borders are translated according to $x_{i+\frac{1}{2}}^{(n+1)} = x_{i+\frac{1}{2}}^{(n)} + \Delta t\, c_{i+\frac{1}{2}}^{(n)}$. New wavelengths $\Delta x_i^{(n+1)} = x_{i+\frac{1}{2}}^{(n+1)} - x_{i-\frac{1}{2}}^{(n+1)}$ yield the new average states $\overline{\psi}_i^{(n+1)} = \left(\Delta x \overline{\psi}\right)_i^{(n+1)} / \Delta x_i^{(n+1)}$. A wave sketch with the discussed variable is presented in Figure 3.1.

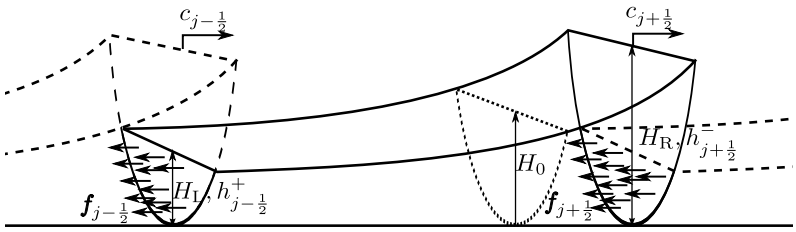

Figure 3.1: A sketch of a wave solution interacting in a wave train.

3.2 An analytical wave model

A local coordinate system $X(x,t)$, moving with celerity $C(x)$, is defined

$$X^{(n)} = x - C^{(n)}t, \qquad \begin{aligned} x_{\mathrm{L}} \le x \le x_{\mathrm{R}}, \\ t_n \le t < t_{n+1}, \end{aligned}$$

[1] To see that both components of $\boldsymbol{f}_{\mathrm{r}}$ are invariants across a shock, let C be the shock speed c and evaluate (3.7a) over an infinitely narrow integral. All but $\boldsymbol{f}_{\mathrm{r}}^+ - \boldsymbol{f}_{\mathrm{r}}^-$ disappears.

where $C^{(n)}$ is generally a function of x, but constant in a steady wave train. Next, translated variables are introduced as $\Phi(X,t) = \phi(x,t)$, reserving upper-case characters for these. Equations (2.2) are now recast in the relative coordinates, yielding

$$\partial_t \boldsymbol{\Psi} + \partial_X \boldsymbol{F}_\mathrm{r} + \boldsymbol{\Psi}\partial_X C = \boldsymbol{S}, \tag{3.7a}$$

$$A_\ell + A_\mathrm{g} = \mathcal{A}, \qquad Q_\ell + Q_\mathrm{g} = \mathcal{Q}, \tag{3.7b}$$

with $\boldsymbol{F}_\mathrm{r} = \boldsymbol{F} - C\boldsymbol{\Psi} = (Q_{\ell,\mathrm{r}}, J_\mathrm{r})^T$ being the fluxes with relative velocities. $Q_{\ell,\mathrm{r}}$ and J_r are of course similar to (3.5) with moving-frame variables.

Note that a non-conservative term $\boldsymbol{\Psi}\partial_X C$ has arisen to represent coordinate stretching. It manifests as a source term because changes in the space within which $\boldsymbol{\psi}$ is conserved are invisible from the stretching reference system.

System (3.7) may also be written in the form of a relative Jacobian $\mathbb{B}_\mathrm{r} = \frac{\partial \boldsymbol{F}}{\partial \boldsymbol{\Psi}} - C\mathbb{I}$, i.e.,

$$\left(\partial_t + \mathbb{B}_\mathrm{r}\partial_x\right)\boldsymbol{\Psi} = \boldsymbol{S} \tag{3.8}$$

where

$$\mathbb{B}_\mathrm{r} = \frac{1}{\rho^*}\begin{pmatrix} (\rho U_\mathrm{r})^* & 1 \\ \kappa^2 & (\rho U_\mathrm{r})^* \end{pmatrix}$$

and

$$\kappa = \sqrt{\frac{\rho^* w_y}{\mathcal{A}'_\ell} - \frac{\rho_\ell \rho_\mathrm{g}}{A_\ell A_\mathrm{g}}\left(U_\mathrm{g} - U_\ell\right)^2}. \tag{3.9}$$

Here, the intrinsic weighting operation

$$\phi^* = \frac{\phi_\ell}{A_\ell} + \frac{\phi_\mathrm{g}}{A_\mathrm{g}}$$

makes its first appearance as an useful shorthand. Eigenvalues of (3.2) are

$$\lambda^\pm_\mathrm{r} = \frac{(\rho U_\mathrm{r})^* \pm \kappa}{\rho^*}. \tag{3.10}$$

3.2.1 The steady profile equation

The profile equation for steady roll-waves are time-invariant, non-stretching solutions of (3.7), i.e., $\partial_t \boldsymbol{\Psi} = \boldsymbol{0}$, $\partial_X C = 0$. Equation (3.7a) then directly yields

$$\frac{\mathrm{d}Q_{\ell,\mathrm{r}}}{\mathrm{d}X} = 0, \qquad\qquad \frac{\mathrm{d}J_\mathrm{r}}{\mathrm{d}X} = S,$$

where the first result implies that $Q_{\ell,\mathrm{r}}$, and therefore also $Q_{\mathrm{g,r}}$, are constant. Applying the chain rule $\frac{\mathrm{d}J_\mathrm{r}}{\mathrm{d}X} = \frac{\mathrm{d}J_\mathrm{r}}{\mathrm{d}H}\frac{\mathrm{d}H}{\mathrm{d}X}$ to the second result yields

$$X' = \frac{J'_\mathrm{r}}{S}, \qquad \text{(steady wave)}. \tag{3.11a}$$

This is the profile equation, inverted. The level height H has been chosen as integration variable and so

$$\phi' = \frac{\mathrm{d}\phi}{\mathrm{d}H}$$

has been defined. Imposing $Q_{k,\mathrm{r}} = \mathrm{const}$, the profile numerator is found to be

$$J'_{\mathrm{r}} = \frac{\mathrm{d}J_{\mathrm{r}}}{\mathrm{d}H} = w_y - \mathcal{A}'_\ell \left(\rho\, U_{\mathrm{r}}^2\right)^* . \tag{3.11b}$$

Relative velocities are of course $U_{k,\mathrm{r}} = U_k - C$. The dynamic frame of the source does not cause any changes as compared to (2.2d), i.e.,

$$S = -w_x - \left[\frac{\mathcal{T}\Sigma}{A}\right]_{\mathrm{g}}^{\ell} + \mathcal{T}_{\mathrm{i}}\Sigma_{\mathrm{i}} \left(\frac{1}{A_\ell} + \frac{1}{A_{\mathrm{g}}}\right). \tag{3.11c}$$

All terms appearing in (3.11a) are functions of H alone.

For the formation of a steady solution to be possible, i.e., for $\partial_t \mathbf{\Psi} \to 0$, the roots of J'_{r} and S must coincide in what is known as the 'critical point' H_0: $J'_{\mathrm{r}}(H_0) = S(H_0) = 0$. The wave height increases monotonically with the region $H < H_0$ being hydraulically supercritical ($\mathrm{sgn}\lambda^- = \mathrm{sgn}\lambda^+$) and $H > H_0$ being subcritical ($\mathrm{sgn}\lambda^- \neq \mathrm{sgn}\lambda^+$). This is the profile equation similar to that presented by Watson [18] (alternatively Johnson in [10].)

The well-known 'viscous Kelvin-Helmholtz' criterion for marginal flow stability [1] can easily be inferred directly from the profile equation (3.11) as a zero-amplitude roll-wave. Even a zero-amplitude wave must contain a critical point H_0. By uniformity, all points in a marginally stable plane flow are critical points. In addition, for the wave to remain at zero amplitude, S in (3.11a) must be at an equilibrium with respect to H. Consequentially, the viscous Kelvin-Helmholtz criterion, as presented in [1], may simply be written

$$S = 0, \qquad S' = 0, \qquad J'_{\mathrm{r}} = 0.$$

The first condition is the hold-up equation, providing the steady, waveless stratified state. The second condition determines the critical wave speed while the third forms the criterion of marginal stability. In this way, viscous, stratified stability theory is a natural component of the wave profile solution; breaking wave solutions does not exist unless the uniformly plane stratified flow solution is unstable.

3.2.2 The stretching profile equation

In contrast to the steady wave solution, $\mathbf{\Psi}$ is here still a function of time, and C and $Q_{\ell,\mathrm{r}}$ are generally not constant within a wave. The state $\mathbf{\Psi}$ is however still approximated as a single variable function in H. For this to be reasonable, the time variation is assumed slow and relatable to the average properties and fluxes. Thus, time dependency is included only indirectly through locally parametric state averages $\mathbf{\Phi}(X,t) \to \mathbf{\Phi}\big(X; \overline{\psi}(t), \boldsymbol{f}_{\mathrm{L}}(t), \boldsymbol{f}_{\mathrm{R}}(t)\big)$ and differentiated as a single variable function.

$C(H; c_{\mathrm{L}}, c_{\mathrm{R}})$ and $Q_{\ell,\mathrm{r}}(H; q_{\ell,\mathrm{L}}, q_{\ell,\mathrm{R}})$ are modelled locally within the wave to remain globally continuous – Section 3.2.3. These should evolve towards constant values as the steady state solution (3.11a) is approached. Phase velocities are given directly from $U_k = Q_{k,\mathrm{r}}/A_k + C$, with $Q_{\mathrm{g,r}} = Q_{\mathrm{m}} - AC - Q_{\ell,\mathrm{r}}$.

The derivative of the state $\mathbf{\Psi} = \left(A_\ell, [\rho\, U]_{\mathrm{g}}^{\ell}\right)^T$, with respect to the single variable H, is

$$\mathbf{\Psi}' = \begin{pmatrix} 1 \\ -\left(\rho\, U_{\mathrm{r,adj}}\right)^* \end{pmatrix} \mathcal{A}'_\ell, \tag{3.12}$$

where the adjusted relative velocities

$$U_{k,\mathrm{r,adj}} = U_{k,\mathrm{r}} - \frac{Q'_{\ell,\mathrm{r}} - A_\ell C'}{\mathcal{A}'_\ell} = U_k - \frac{Q'_\ell}{\mathcal{A}'_\ell} \tag{3.13}$$

have been introduced. Equation (3.8) may now be written

$$\left(\boldsymbol{\Psi}'\partial_t + \mathbb{B}_{\mathrm{r}}\boldsymbol{\Psi}'\partial_x\right) H = \begin{pmatrix} 0 \\ S - S_{\mathrm{trans}} \end{pmatrix}, \tag{3.14}$$

where S_{trans} is an artificial source representation of rest terms $\rho^* \left(\partial_t Q_{\ell,\mathrm{r}} + A_\ell \partial_t C\right)$ from the slow transient – it will be discussed shortly. Eliminating $\partial_t H$ between the two equation components of (3.14), one obtains the stretchable inversed profile equation

$$X' = \frac{J'_{\mathrm{r,adj}}}{S - S_{\mathrm{trans}}}, \tag{3.15}$$

with

$$J'_{\mathrm{r,adj}} = w_y - \mathcal{A}'_\ell \left(\rho\, U^2_{\mathrm{r,adj}}\right)^*. \tag{3.16}$$

Note that if the flow has reached a steady state in which $[q_{\ell,\mathrm{r}}]^{\mathrm{R}}_{\mathrm{L}} = [c]^{\mathrm{R}}_{\mathrm{L}} = 0$, then both $Q_{\ell,\mathrm{r}}$ and C are constants (see Section 3.2.3.) One has from (3.13) that $J'_{\mathrm{r,adj}} = J'_{\mathrm{r}}$ and (3.15) becomes identical to the steady discontinuous solutions (3.11), provided $S_{\mathrm{trans}} \to 0$.

A truly steady wave in which $S_{\mathrm{trans}} = 0$ and $\partial_t \boldsymbol{\Psi} = 0$ also implies that the roots of J'_{r} and S coincide at the critical point H_0, as explained in Section 3.2.1. In evolving waves, on the other hand, the roots of $J'_{\mathrm{r,adj}}$ and S will not coincide perfectly. The quite simple means of making the profile integrable is here to let the S_{trans} term, representing the transient residual, provide the degree of freedom needed for accomplishing the double root. S_{trans} is made a spatial constant within each wave, expressing the discrepancy between the two roots. Precisely, $S_{\mathrm{trans}} = S(H_0)$ where H_0 is the root of $J'_{\mathrm{r,adj}}$.

Johnson et. al. [10] chose the friction multiplier m_{x} such that the double root was achieved, rather than using an artificial source term. The present approach was chosen in order to make the method independent of the friction closure.

Note that if second order differential terms are to be included into the profile model, for instance turbulent shear terms as in [12], the profile may no longer be monotonic and the variable inversion $H(X) \to X(H)$ no longer possible.

3.2.3 Modelling 'in the small' – $Q_{\ell,\mathrm{r}}(H)$ and $C(H)$

In this section the choices for the modelled discharge rate $Q_{\ell,\mathrm{r}}$ and translation velocity C are discussed. These choices then directly govern the transient $\partial_t A_\ell$ in the strip $[t_n, t_{n+1}\rangle$ through the mass equation in (3.7a).

$Q_{\ell,\mathrm{r}}$ and C are made globally continuous and locally linear in their individual variable ξ, that is

$$\phi = \phi_{\mathrm{L}} + [\phi]^{\mathrm{R}}_{\mathrm{L}} \frac{\xi_\phi - \xi_{\phi,\mathrm{L}}}{[\xi_\phi]^{\mathrm{R}}_{\mathrm{L}}}, \qquad \phi \in \{Q_{\ell,\mathrm{r}}, C\}. \tag{3.17}$$

The ξ's are chosen as

$$\xi_{Q_{\ell,\mathrm{r}}} = A_\ell^{3/2}\left(\mathcal{A}'_\ell\right)^{-1/2}, \qquad \xi_C = 1/A_\ell.$$

The choice for $\xi_{Q_{\ell,\mathrm{r}}}$ is motivated by the consideration that changes in $Q_{\ell,\mathrm{r}}$ should be consistent with the characteristic speeds (3.10), simplified in assuming $\rho_\ell \gg \rho_\mathrm{g}$ (the characteristics of the shallow water equations.)

ξ_C is chosen considering the adjusted relative liquid convection velocity $U_{\ell,\mathrm{r,adj}} = \big(Q_{\ell,\mathrm{r}} - A_\ell \frac{\mathrm{d}Q_{\ell,\mathrm{r}}}{\mathrm{d}A_\ell} - A_\ell^2 \frac{\mathrm{d}C}{\mathrm{d}A_\ell}\big)/A_\ell$ active in $J'_{\mathrm{r,adj}}$, seeking to make the influence of coordinate stretching uniform.

These sub-models do affect the wave dynamics notably, and better alternatives are likely to exist.

3.3 Finding the Correct Profile Solution

Expression (3.15) gives the inverse wave profile as function of H. The wave profile should be consistent with the average wave cell properties, i.e., wavelength, mass and momentum from the integral equations, that is

$$\left(1, \overline{a_\ell}, [\rho\overline{u}]_\mathrm{g}^\ell\right) = \frac{1}{\Delta x}\int_{h_\mathrm{L}}^{h_\mathrm{R}} \left(1, A_\ell, [\rho\, U]_\mathrm{g}^\ell\right) \frac{J'_{\mathrm{r,adj}}}{S - S_{\mathrm{trans}}}\,\mathrm{d}H. \tag{3.19}$$

These three conditions, together with the shock condition (3.6), are sufficient to uniquely determine the shock states $\{h^+, h^-, q_\ell, c\}_{i+\frac{1}{2}}$. A multi-dimensional root search algorithm is employed for the job. [2]

The momentum flux $j_{\mathrm{r,L}}$ through the left face of the control volume is computed $j_{\mathrm{r,L}} = J_\mathrm{r}(H_\mathrm{L}, q_{\ell,\mathrm{L}}, c_\mathrm{L})$, and similar for the right face. J_r will then remain globally continuous since c was defined in (3.6) to maintain the momentum invariant across shocks. Likewise, $Q_{\ell,\mathrm{r}}$ is globally continuous from (3.17). Finally, the average source term is

$$\overline{s} = \overline{S} = \frac{1}{\Delta x}\int_{h_\mathrm{L}}^{h_\mathrm{R}} S\,\frac{J'_{\mathrm{r,adj}}}{S - S_{\mathrm{trans}}}\,\mathrm{d}H.$$

The profile itself is then given by

$$X(h) = X_\mathrm{L} + \int_{h_\mathrm{L}}^{h} \frac{J'_{\mathrm{r,adj}}}{S - S_{\mathrm{trans}}}\,\mathrm{d}H; \quad h_\mathrm{L} \le h \le h_\mathrm{R}.$$

Main conditions for a physical wave profile solution are

$$h_\mathrm{L} < H_0 < h_\mathrm{R} \tag{3.20a}$$
$$J'_{\mathrm{r,adj}} > 0, \qquad H > H_0 \tag{3.20b}$$
$$S - S_{\mathrm{trans}} > 0, \qquad H > H_0 \tag{3.20c}$$
$$J'_{\mathrm{r,adj}} < 0, \qquad H < H_0 \tag{3.20d}$$
$$S - S_{\mathrm{trans}} < 0, \qquad H < H_0 \tag{3.20e}$$
$$C < U_\ell, \qquad h_\mathrm{L} < H < h_\mathrm{R} \tag{3.20f}$$

[2] The CAW method was programmed in the MATLAB language; built-in functions `integrate` and `fsolve` of version R2013b were used to evaluate (3.19) and to search for the roots, respectively.

Further details on the conditional nature of S, J'_{r} and the shock relation (3.6) is provided in [11, 10]. Conditions (3.20a) and (3.20b) imply that h_{R} must be less than the upper root of $J'_{\mathrm{r,adj}}$, at which $\frac{\mathrm{d}H}{\mathrm{d}X} \to \infty$. Likewise, (3.20a) and (3.20e) implies that h_{L} must be greater than the lower root of $S - S_{\mathrm{trans}}$, at which $\frac{\mathrm{d}H}{\mathrm{d}X} \to 0$.

3.4 Simulation routine

A simultaneous and a sequential solver approach will presently be described. The main distinction is that the simultaneous procedure requires the solution of one $4 \times N$-dimensional profile problem every time step, N being the number of waves, while the sequential procedure requires the solution of N three-dimensional problems.

3.4.1 Simultaneous solver

Each wave in a wave train will provide a shock front (jump) and append four variables (h^+, h^-, $q_{\ell,\mathrm{r}}$ and c) to the system. The shock condition (3.6) couples the individual profiles such that the profile of one wave is mutually dependent on the profile of its neighbouring waves. The number of variables in the coupled system is four times the number of distinct shocks i.e., $\{h^+, h^-, q_{\ell,\mathrm{r}}, c\}_{i+\frac{1}{2}}$, $i = 1 \ldots N$.
Figure 3.2 provides an algorithmic illustration of the simulation procedure.

3.4.2 Sequential solver

If, on the other hand, the wave solutions are decoupled by instead using the wave velocities from the previous time step, the chained wave system will consist of separate three-dimensional single-wave problems with the variables $\{h_{\mathrm{L}}, h_{\mathrm{R}}, q_{\mathrm{r},\ell,\mathrm{L}}\}_i$. $Q^{(n)}_{\ell,\mathrm{r}}$ from (3.17) may be constructed using the old differences $[q_\ell]_{\mathrm{L}}^{\mathrm{R}^{(n-1)}}$ together with $q^{(n)}_{\mathrm{r},\ell,\mathrm{L}}$. An algorithmic illustration is given in Figure 3.3. The downside of a sequential procedure is that it is prone to numerical oscillations due to the lag in celerity information. Under-relaxation of c, performed in the manner $c^{(n)} := rc^{(n-1)} + (1-r)\, c^{(n)}$, r being the relaxation factor, is an effective way of stabilising the sequential routine. Measures like reducing the time step and iterating on the next time level also improve stability, though these measures also reduce the simulation efficiency.

3.5 Implementation and management

The CAW simulator programme is implemented using object oriented programming with wave and shock objects arranged sequentially in a linked list. All flow objects are also linked to the main pipe object holding properties like pipe inclination and diameter, gathered relative to the flow objects' positions during runtime.

The CAW method requires an initial set of wavelengths. This must either be supplied as user input or retrieved from direct simulations (Section 4.)
Wave mergers, or coalescences, are identified from the collision of shocks or the diminishment of the shock height. In such events, two wave objects must merge. Mergers involve compounding the conserved integral properties into a new single wave object which covers the same spatial interval.

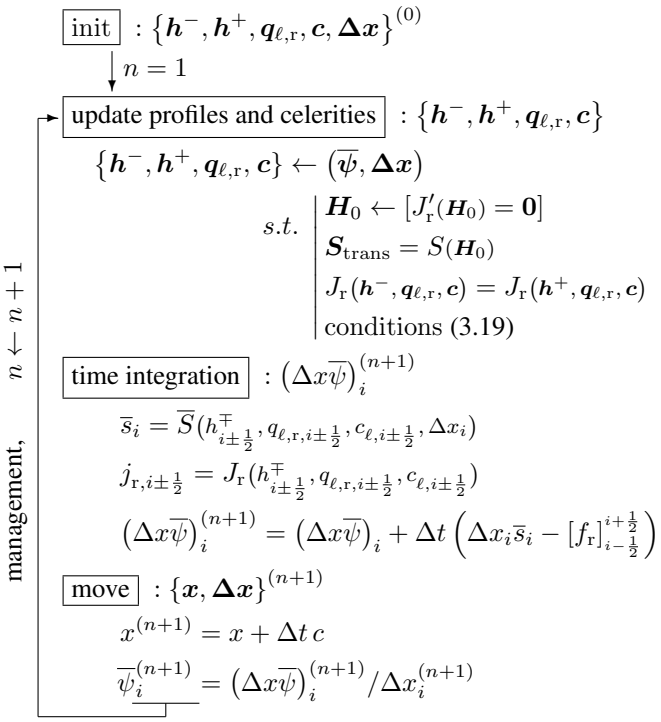

Figure 3.2: Simulation procedure. Profiles solved simultaneously. Time index (n) dropped. Vectors indicate collected shock data.

4 VALIDATION: WAVE CAPTURING THROUGH FINE DISCRETISATION

For validation, the target equations (2.2) are also solved through direct discretisation on a fixed uniform grid.

A number of the simpler common schemes were tested. Out of these, the simplest alternative, an explicit, non-staggered, first order upwind (or donor cell) scheme was preferred on the basis of simplicity. This is used for in all numerical comparisons with the number of grid cells equalling 3000 and the liquid-based CFL number equalling 0.5. For completeness, the discretised equations are presented in (4.1):

$$a_{\ell,i}^{(n+1)} = a_{\ell,i}^{(n)} - \frac{\Delta t}{\Delta x}\left(q_i^{(n)} - q_{i-1}^{(n)}\right), \tag{4.1a}$$

$$u_{\ell,i}^{(n+1)} = \left(\rho_\ell + \rho_{\mathrm{g}}\frac{a_{\ell,i}^{(n+1)}}{a_{\mathrm{g},i}^{(n+1)}}\right)^{-1} \times \left[\frac{\rho_{\mathrm{g}}\,\mathcal{Q}}{a_{\mathrm{g},i}^{(n+1)}} + \left[\rho\, u_i^{(n)}\right]_{\mathrm{g}}^{\ell} - \frac{\Delta t}{\Delta x}\left(j_i^{(n)} - j_{i-1}^{(n)}\right) + s_i^{(n)}\right], \tag{4.1b}$$

with q_ℓ and j given in (2.2c) and s in (2.2d). Simulations performed with (4.1) will simply be referred to as 'direct simulations' in the following discussion.

Although the direct simulations are finely resolved, one should keep in mind that they too are associated with inaccuracies from numerical diffusion and dispersion.

5 NUMERICAL EXPERIMENTS

This work contains a large number of parameters. In the interest of briefness the parameters listed in Table 1 will remain fixed for all numerical experiments. Fluid parameters correspond

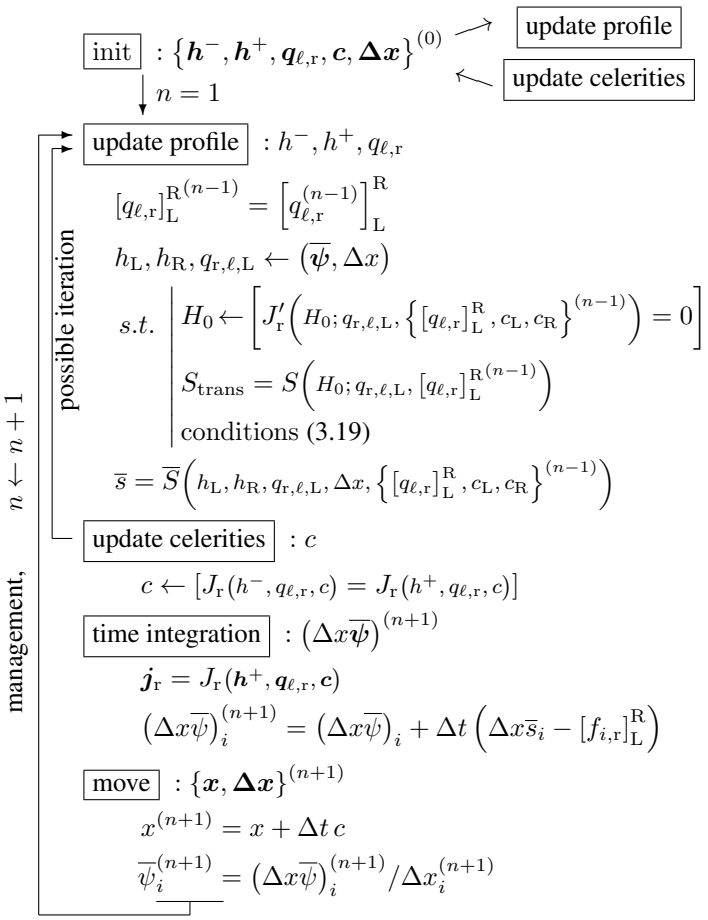

Figure 3.3: Simulation procedure. Profiles solved sequentially. Time index (n) dropped. Vectors indicate collected shock data.

to air-water flow in atmospheric conditions. Boundary conditions are made periodic (cyclic) for all test cases.

ρ_ℓ	998	$\mathrm{kg/m^3}$
ρ_g	1.205	$\mathrm{kg/m^3}$
ν_ℓ	1.005E-6	$\mathrm{m^2/s}$
ν_g	1.50E-5	$\mathrm{m^2/s}$
m_x	5.0	–
d	0.078	m
$q_\ell^{(0)}/\mathcal{A}$	0.25	$\mathrm{m/s}$

Table 1: Fixed parameters.

5.1 Simulations where the initial CAW profiles are used as the initial conditions for the direct simulation.

The first set of simulations are presented in Figure 5.1. Here, CAW simulations consist of two waves with initial length $\Delta x^{(0)} = 10\,d$ and $\Delta x^{(0)} = 20\,d$. A direct simulation runs alongside the CAW simulation in each case. Initial conditions in the direct simulations are taken as point values of the initial profile solution of the CAW. At $t > 0$ the two simulation methods run independent of each other. Initial superficial velocities of the gas phase are $q_\mathrm{g}^{(0)}/\mathcal{A} = 10.0\,\mathrm{m/s}$ in Subfigure (a) and (b), and $q_\mathrm{g}^{(0)}/\mathcal{A} = 11.0\,\mathrm{m/s}$ in Subfigure (c). The mixture rate remains unchanged from its initial value through all cases, that is $\mathcal{Q} \equiv q_\ell + q_\mathrm{g} = q_\ell^{(0)} + q_\mathrm{g}^{(0)}$.

Subfigure (a) shows the profile development in a one degree upwards inclined pipe. Wave profiles remain similar throughout the simulation, and wave coalescence occurs in close proximity in time and space. The predicted rate at which the shorter wave is eaten by the longer one is seen to differ more as the distance between wave fronts decreases. This feature may be caused by the diffusive properties of the simple direct simulation scheme, or it can be caused by an increase in the artificial source S_trans required to maintain the quasi-steady approximation in the CAW method. A third possible explanation for the slight discrepancy is that the sub-models of Section 3.2.3 are not optimal.

In Subfigure (b), the pipe inclination is one degree downwards. This manifests in higher waves and faster coalescence. (Waves pass the periodic boundaries many times in between snapshots.) The rate of coalescence is still greater in Subfigure (c), where the gas rates have been increased. The wave resulting from this wave merger is unstable, which from a modelling perspective can be interpreted at the formation of a momentary slug. In the direct simulation, this is seen as numerical instability; a sudden exponential and non-physical growth at the wave tip (also occurring in Figures 5.3,) leading to a simulation breakdown. In the CAW simulation, the instability is manifested in that no single monotone profile solution fitting the average properties exists.

Figure 5.2 presents the time evolution of the artificial source term S_trans for the two stable cases, Figure 5.1a and b. S_trans is largest initially and just before and just after a wave coalescence. The larger values of S_trans prior to a coalescence may contribute to the discrepancy in predicted celerities, as mentioned above. After coalescence, S_trans quickly diminishes to-

wards zero, meaning that the solution becomes identical to the steady wave solution presented in Section 3.2.1.

5.2 Simulations where the initial conditions of the CAW simulation are collected from a developing direct simulation.

A similar case set-up is presented in Figures 5.3 and 5.4 with a horizontal pipe. These CAW simulations are initiated with the average wave properties gathered from an intrinsically developing direct simulation. The direct simulation was initially uniform apart from a tiny, pointwise random disturbance. Instantaneous data was then stored at $t = 30\,\mathrm{s}$, before the growing waves began to break. Resetting the time to $t = 0$, CAW simulations are initiated by partitioning the direct simulation domain and averaging the properties within these partitions. The criterion for a wave partition is that it forms the midpoint between a local left peak and local right trough in liquid fraction. These wave are still developing, as can be seen from the initial profiles at $t = 0$. Figure 5.3 shows wave profile snapshots and Figure 5.4 displays the wavelengths development in time. Subfigures 5.3a and 5.4a present a simulation with sequentially computed CAW profiles (Section 3.4.2.) This simulation has been computed with a 90% under-relaxation when updating the wave celerities, keeping it numerically stable. The flow pattern evolves slowly and does not appear to be greatly affected by the considerable relaxation.

Subfigures 5.3b and 5.4b present this same test case when adopting the simultaneous solution procedure (Section 3.4.1.) Average states $\overline{\psi}$ are compared in Figure 5.5. The time and location of wave mergers are here in good agreement, keeping in mind the these simulations ran independently of each other before direct simulation waves started to break.

Finally, Figure 5.6 compares the two-wave development in a range of pipe inclinations, (a), for gravity driven flows, and, (b), for pressure driven flows.

5.3 Multiple waves in alternating pipe geometry

Finally, a larger simulation with multiple waves is performed in a snake-like pipe configuration. The pipeline geometry is shown in Table 2. $q_{\mathrm{g}}^{(0)}/\mathcal{A} = 9\,\mathrm{m/s}$. Periodic boundary conditions make this configuration continuous.

Pipe	1	2	3	4	5	6	7	8	9	10
θ	-.1°	-.3°	-.5°	-.3°	-.1°	.1°	.3°	.5°	.3°	.1°
L	10	10	20	10	10	10	10	20	10	10

Table 2: Pipeline geometry

In order to avoid disturbing the profile search routine, changes in pipe inclination are accounted for by approximating a constant inclination in the profile equation. This inclination is computed from the fraction of wave found within each pipe segment. CAW profiles will thus react instantaneously to the changing inclination, inertia being supplied only though the average state. The sequential solver (Figure 3.3) is used with 95% under-relaxation.

Figure 5.7 presents the time evolution from a 12-wave simulation in a 120 diameter long domain. The two predictions remain fairly consistent throughout the simulation. Alternating pipe inclinations are manifested as a wavy evolution in the wavelength plot, Figure 5.8.

(a) $\theta = +1°$, $q_g^{(0)}/\mathcal{A} = 10\,\mathrm{m/s}$.

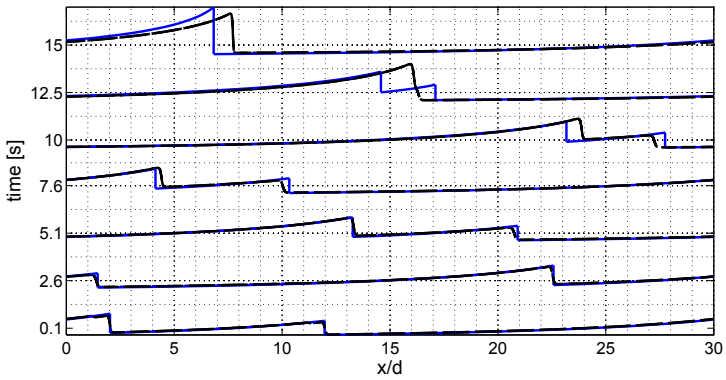

(b) $\theta = -1°$, $q_g^{(0)}/\mathcal{A} = 10\,\mathrm{m/s}$.

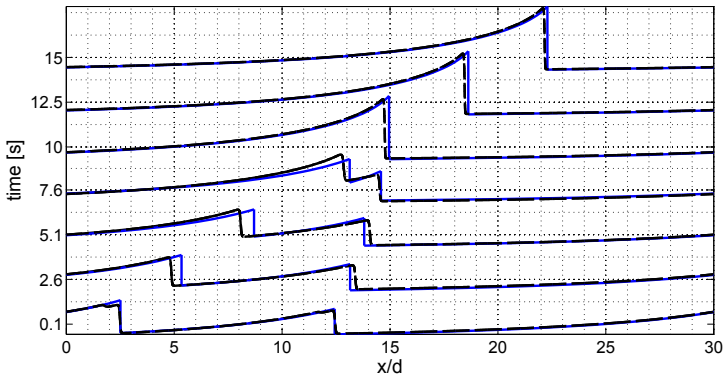

(c) $\theta = -1°$, $q_g^{(0)}/\mathcal{A} = 11\,\mathrm{m/s}$.

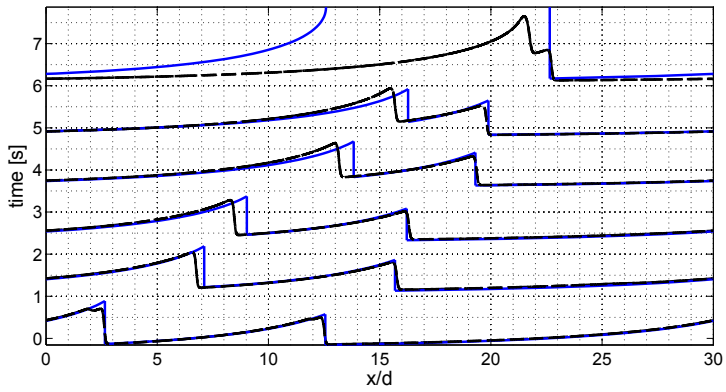

Figure 5.1: Double wave simulation using the simultaneous solution procedure. The initial state of the direct simulations is taken from the initial solutions of the analytical waves. Solid line: CAW, stippled line: direct simulation.
$\Delta x^{(0)} \in \{10\,d, 20\,d\}$. Wave heights H ranges from around $0.1\,d$ to $0.3\,d$ before coalescence. (Waves pass through boundaries many times between each profile visualisation.)

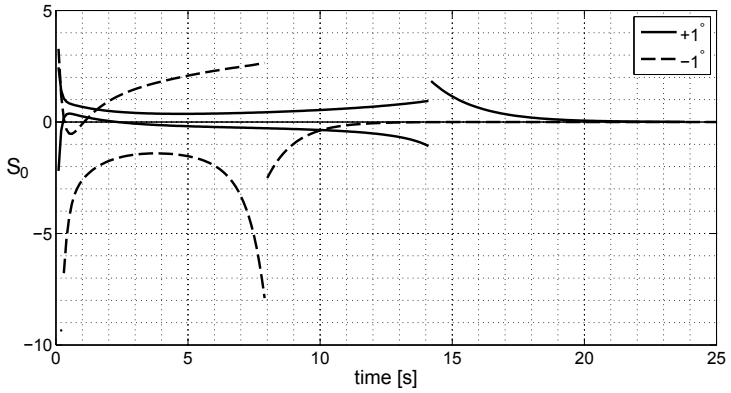

Figure 5.2: Artificial source S_{trans}. $q_{\text{g}}^{(0)}/\mathcal{A} = 10.0\,\text{m/s}$, $\theta = \pm 1°$, cf. Figure 5.1a and b.

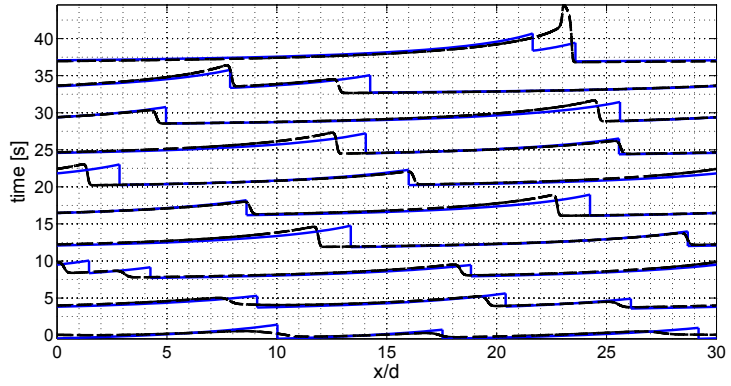

(a) Sequential procedure. 90% relaxation.

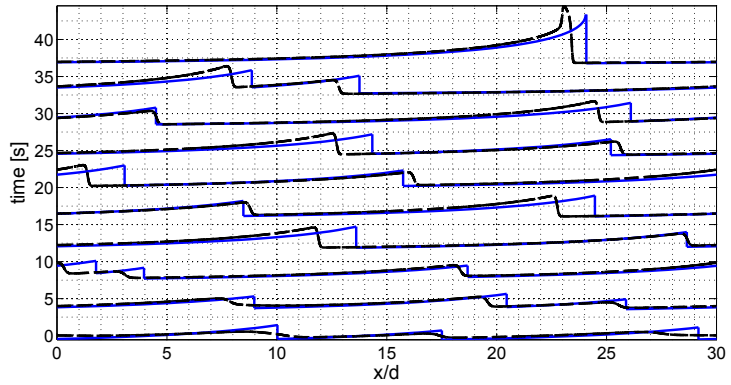

(b) Simultaneous procedure. (No relaxation.)

Figure 5.3: Profile development in time. The initial average states of the analytical wave simulation is computed by averaging partitions of a direct simulation at $t = 30\,\text{s}$. Solid line: CAW, stippled line: direct simulation.
$q_{\text{g}}^{(0)}/\mathcal{A} = 11\,\text{m/s}$, $\theta = 0°$.

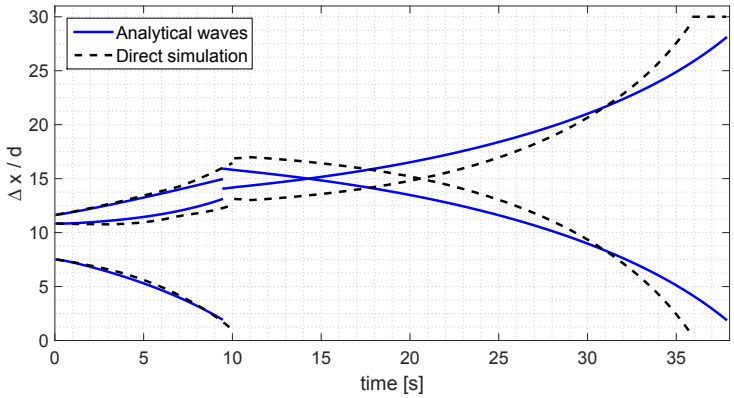

(a) Sequential procedure. $Q_{\ell,\mathrm{r}}(H)$ and $C(H)$, as per Section 3.2.3. 90% relaxation.

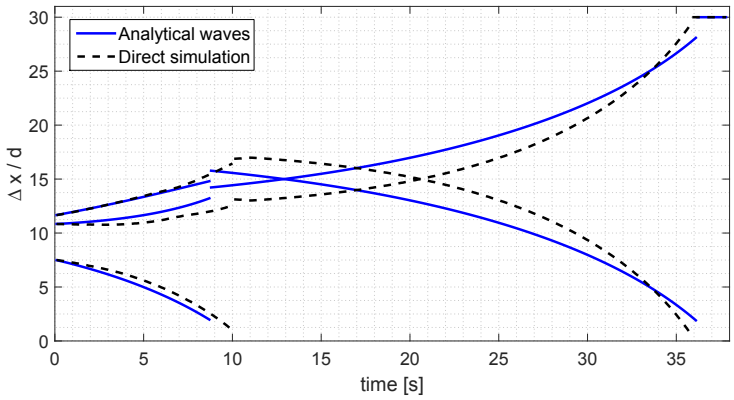

(b) Simultaneous procedure. $Q_{\ell,\mathrm{r}}(H)$ and $C(H)$, as per Section 3.2.3. (No relaxation.)

Figure 5.4: Wavelength development in time, presented as $\Delta x/d$. Cf. Figure 5.3.

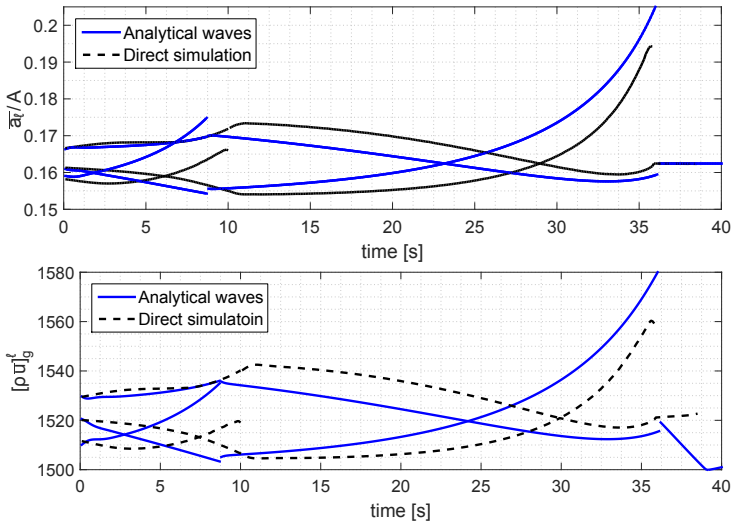

Figure 5.5: $\overline{a_\ell}/A$ and $[\rho\,\overline{u}]_{\mathrm{g}}^{\ell}$. Simultaneous procedure, cf. Figure 5.3b

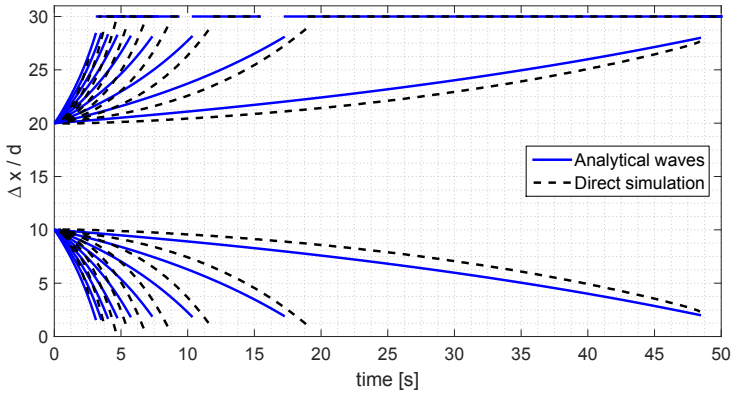

(a) No gas present. $\theta \in \{-1.5°, -2.0°, \ldots, -5.5°\}$ where the lengths of the curbed lines on the 'fan' decreases with increasing inclination.

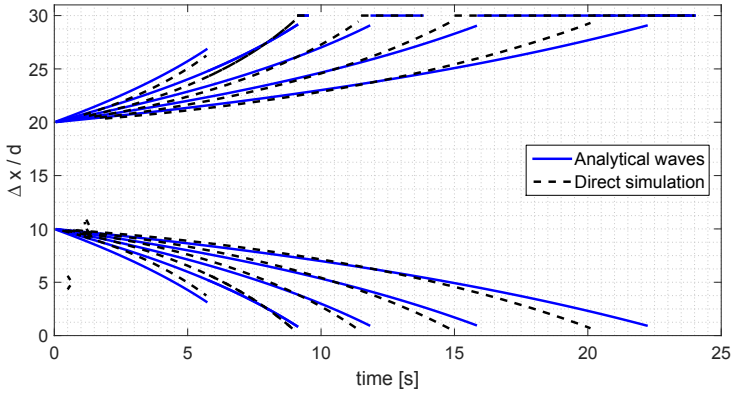

(b) $\theta = 0°$. $q_g^{(0)}/\mathcal{A} \in \{8\,\mathrm{m/s}, 9\,\mathrm{m/s}, \ldots, 12\,\mathrm{m/s}\}$ where the lengths of the curbed lines on the 'fan' decreases with increasing superficial gas velocity.

Figure 5.6: Wavelength plot. Simultaneous procedure.

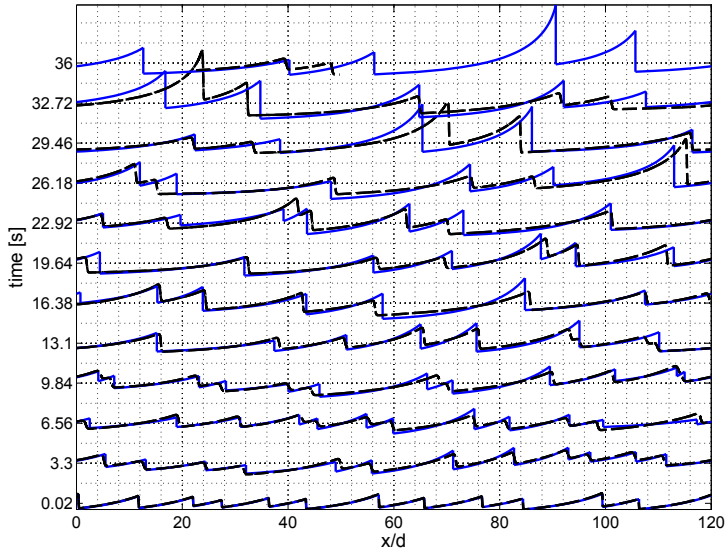

Figure 5.7: Multiple waves in the pipeline configuration of Table 2; profile evolution. Solid line: CAW, stippled line: direct simulation.

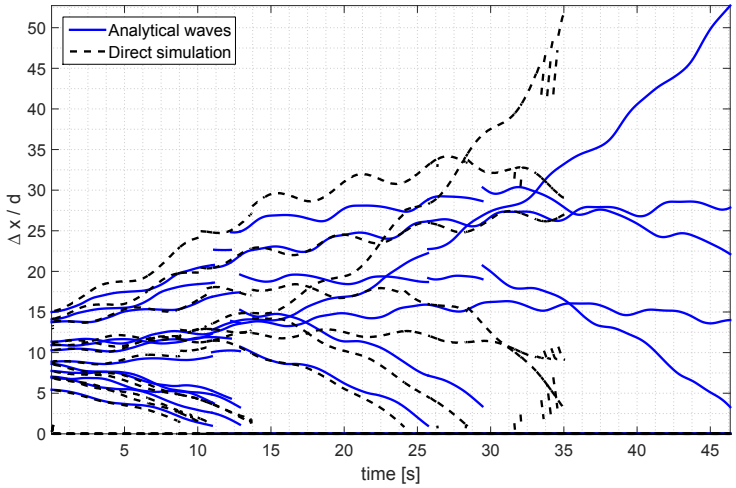

Figure 5.8: Multiple waves in the pipeline configuration of Table 2, cf. Figure 5.7; wavelength evolution.

The higher waves coalesce quicker in the capturing simulation than in the CAW during the later stages of the simulation, similar to what was observed in the two-wave simulations. Coalescence of the two highest waves takes place around $t = 35\,\mathrm{s}$ in the direct simulation, resulting in an unstable wave and the subsequent simulation break-down. This happens about ten seconds later in the CAW simulation.

Average variables $\overline{\psi}$ are again plotted against time in Figure 5.9. Oscillations of these average variables are quite consistent, despite the significant under-relaxation of the sequential CAW solver.

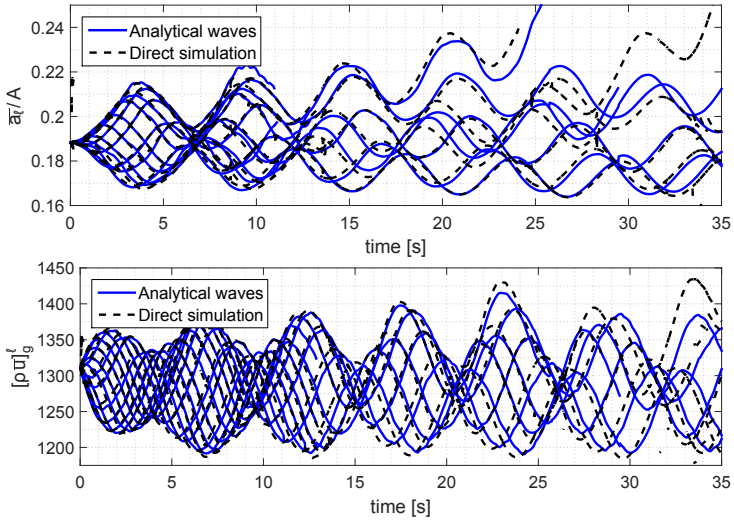

Figure 5.9: Average wave properties $\overline{\psi} = \langle \overline{a_\ell}, [\rho\,\overline{u}]_g^\ell \rangle$ cf. Table 2 and Figure 5.7

6 POTENTIAL AND EFFICIENCY

Tests presented in the previous section were of a basic nature, evaluating the main principle that analytical wave solutions would evolve appropriately if put into a dynamic frame. Obviously, the applicability such principles is tightly hinged on the degree to which defined structures (waves) are physically present.

Regarding efficiency, the bottleneck of the CAW method, as presented here, is the profile reconstruction of Section 3.3, implemented with a multi-dimensional root search algorithm. The main computational cost within this profile search routine is in turn the numerical profile integrations for retrieving average wave properties. Such costly routines can be acceptable only if that cost can be regained through significantly fewer cells and larger time steps. Simpler models, or profile approximations, which provide algebraically pre-integrable expressions would alleviate the computational cost significantly.

7 CONCLUSIONS

A simulation concept which takes advantage of naturally occurring flow structures has been presented and tested using a method of dynamically chained analytical waves. Results compare favourably with fully resolved direct simulations of the same state equation set.

In particular, the tested method seems capable of predicting wave speeds, wave evolution and wave coalescences with reasonable accuracy in time and space. The method shows the same

stability behaviour as in the fully resolved simulations, and appears to be well adopted for the range of flow parameters within which the roll-wave phenomenon is set to occur. Prediction accuracy is likely to improve with further method development.

Predictions are made using vastly larger grid cells and time steps than what is required with conventional finite-volume methods. Still, better ways of searching for profile solutions seems to be necessary for the method to become truly efficient. The method also requires initial wavelengths as input. However, once some initial wavelengths have been given, or extracted from a direct simulation, the wave regime develops either towards an appropriate steady state or a flow regime transition.

Acknowledgements

This work is financed by The Norwegian University of Science and Technology (NTNU) as a contribution to the Multiphase Flow Assurance programme (FACE.) The author thanks Kontorbamse for the inspirational support.

REFERENCES

[1] D. Barnea and Y. Taitel. Interfacial and structural stability of separated flow. *International Journal of Multiphase Flow*, 20(supplissue):387 – 414, 1994/08/.

[2] D. Biberg. A mathematical model for two-phase stratified turbulent duct flow. *Multiphase Science and Technology*, 19(1):1 – 48, 2007.

[3] R.R. Brock. Development of roll-wave trains in open channels. *American Society of Civil Engineers, Journal of the Hydraulics Division*, 95(HY4):1401 – 1427, 1969.

[4] B.S. Brook, S.A.E.G. Falle, and T.J. Pedley. Numerical solutions for unsteady gravity-driven flows in collapsible tubes: evolution and roll-wave instability of a steady state. *Journal of Fluid Mechanics*, 396:223 – 56, 1999/10/10.

[5] Zhixian Cao, Penghui Hu, Kaiheng Hu, Gareth Pender, and Qingquan Liu. Modelling roll waves with shallow water equations and turbulent closure. *Journal of Hydraulic Research*, 0(0):1–17, 0.

[6] A. De Leebeeck and O.J. Nydal. Simulation of large amplitude waves in a slug tracking scheme compared to roll wave experiments at high pressure. *International Journal of Multiphase Flow*, 36(1):40 – 50, 2010.

[7] R.F. Dressler. Mathematical solution of the problem of rollwaves in inclined open channels. *Communications on Pure and Applied Mathematics*, 2:149 – 194, 1949/06/.

[8] D. Gidaspow. Multiphase flow and fluidization. *Journal of Fluid Mechanics*, 287:405 – 405, 1995.

[9] H. Holmås. Numerical simulation of transient roll-waves in two-phase pipe flow. *Chemical Engineering Science*, 65(5):1811 – 25, 2010/03/01.

[10] George W. Johnson, Arnold F. Bertelsen, and Jan Nossen. A mechanistic model for roll waves for two-phase pipe flow. *AIChE Journal*, 55(11):2788 – 2795, 2009.

[11] G.W. Johnson. *A Stuy of Stratified Gas-Liquid Pipe Flow*. PhD thesis, Univ. Oslo, 2005. dr. scient.

[12] G.W. Johnson, J. Nossen, and A.F. Bertelsen. A comparison between experimental and continuous theoretical roll waves in horizontal and slightly inclined pipes at high pressure. pages 643 – 655, Barcelona, Spain, 2005.

[13] Jr. Lahey, R.T. Void wave propagation phenomena in two-phase flow (kern award lecture). *AIChE Journal*, 37(1):123 – 35, 1991/01/.

[14] M. Miya, D.E. Woodmansee, and T.J. Hanratty. A model for roll waves in gas-liquid flow. *Chemical Engineering Science*, 26(11):1915 – 31, 1971/11/. liquid film;high speed gas flow;flow surges;roll waves;height;wall shear stress;gas pressure;mathematical model;.

[15] G.L. Richard and S.L. Gavrilyuk. A new model of roll waves: Comparison with brock's experiments. *Journal of Fluid Mechanics*, 698:374 – 405, 2012.

[16] Y. Taitel and A.E. Dukler. A model for predicting flow regime transitions in horizontal and near horizontal gas-liquid flow. *AIChE Journal*, 22(1):47 – 55, 1976/01/.

[17] H. A. Thomas. The propagation of waves in steep prismatic conduits. In *Hydraulics Conf.*, pages 214–229, Carnegie Institute of Technology, Pittsburgh, 1939.

[18] M. Watson. Wavy stratified flow and the transition to slug flow. In C.P. Fairhurst, editor, *Multi-phase Flow – Proceedings of the 4th International Conference*, pages 495–512, Cranfield, UK, 1989.